

Spinning pupil aberration measurement for anisoplanatic deconvolution: supplement

DANIELE ANCORA,¹  TOMMASO FURIERI,^{2,3} STEFANO BONORA,^{2,*}
AND ANDREA BASSI¹ 

¹Politecnico di Milano, Department of Physics, piazza Leonardo da Vinci 32, 20133 Milan, Italy

²National Council of Research of Italy, Institute of Photonics and Nanotechnology, via Trasea 7, 35131, Padova, Italy

³University of Padova, Department of Information Engineering, Via Gradenigo 6, 35131, Padova, Italy

*Corresponding author: stefano.bonora@pd.infn.cnr.it

This supplement published with The Optical Society on 14 June 2021 by The Authors under the terms of the [Creative Commons Attribution 4.0 License](https://creativecommons.org/licenses/by/4.0/) in the format provided by the authors and unedited. Further distribution of this work must maintain attribution to the author(s) and the published article's title, journal citation, and DOI.

Supplement DOI: <https://doi.org/10.6084/m9.figshare.14617668>

Parent Article DOI: <https://doi.org/10.1364/OL.427518>

Spinning Pupil Aberration Measurement for anisoplanatic deconvolution

DANIELE ANCORA,¹ TOMMASO FURIERI,^{2,3} STEFANO BONORA,^{2,*} ANDREA BASSI¹

¹Politecnico di Milano, Department of Physics, piazza Leonardo da Vinci 32, 20133 Milan, Italy

²National Council of Research of Italy, Institute of Photonics and Nanotechnology, via Trasea 7, 35131, Padova, Italy

³University of Padova, Department of Information Engineering, Via Gradenigo 6, 35131, Padova, Italy

*Corresponding author: stefano.bonora@pd.ifn.cnr.it

Supplementary material

The process of wavefront measurement through SPAM is conceptually identical to the Shack-Hartman Wave Front Sensing. To measure the wavefront on the whole pupil the system scans it with a sub aperture in m positions (Fig. 1a) and acquires the image shift.

For example, with an aberration common to the whole field of view, for each sub-pupil position we would observe a rigid displacement of the whole image. Conversely, with a field-dependent aberration, the displacement is position-dependent leading to a distortion of the image.

1	2	3
4	5	6
7	8	9

Fig. S1: Example of division of the field of view. For simple visualization the case $N = 3$ is shown, corresponding to $k=3 \times 3$ sectors.

In order to measure the aberration in each position of the field of view, we virtually divide the detector into $k=N^2$ equally spaced sectors and then we compute the displacement of the image in each sector relative to the image taken with the sub-pupil in the central position.

Therefore, the displacement measured with the i th sector is a column vector whose entries are the x and y displacement information, namely:

$$\vec{\Delta S}_i = \begin{pmatrix} \Delta S_{x,1,i} \\ \vdots \\ \Delta S_{x,m,i} \\ \Delta S_{y,1,i} \\ \vdots \\ \Delta S_{y,m,i} \end{pmatrix}.$$

The displacement is arranged in a column vector ΔS :

$$\Delta s = \begin{pmatrix} \Delta s_{x,1,1} \\ \vdots \\ \Delta s_{x,m,1} \\ \Delta s_{y,1,1} \\ \vdots \\ \Delta s_{y,m,1} \\ \vdots \\ \vdots \\ \vdots \\ \Delta s_{x,1,k} \\ \vdots \\ \Delta s_{x,m,k} \\ \Delta s_{y,1,k} \\ \vdots \\ \Delta s_{y,m,k} \end{pmatrix} = \begin{pmatrix} \overrightarrow{\Delta s_1} \\ \vdots \\ \overrightarrow{\Delta s_9} \end{pmatrix}$$

We finally convert Δs into wavefront gradients as:

$$\nabla W_i = \frac{PixWidth}{f} \Delta s_i$$

where $PixWidth$ is the dimension of the camera pixel, f is the tube lens focal length and i is the field referred to the i_{th} image region. The wavefront is computed using modal reconstruction algorithm [1].

Wavefront reconstruction accuracy vs sub pupil Dimensions

We carried out some simulations to choose the best sub-pupil dimension for an optimal wavefront reconstruction.

We generated a wavefront with 0.4 waves (@530nm) of each Zernike coefficient from the 3rd to the 14th (Fig S2) and, starting from this wavefront, we run the wavefront measurement algorithm using different sub-pupil dimensions. To measure the performance of the various configurations the reconstructed wavefront was then subtracted from the real one. The results are shown in table T1.

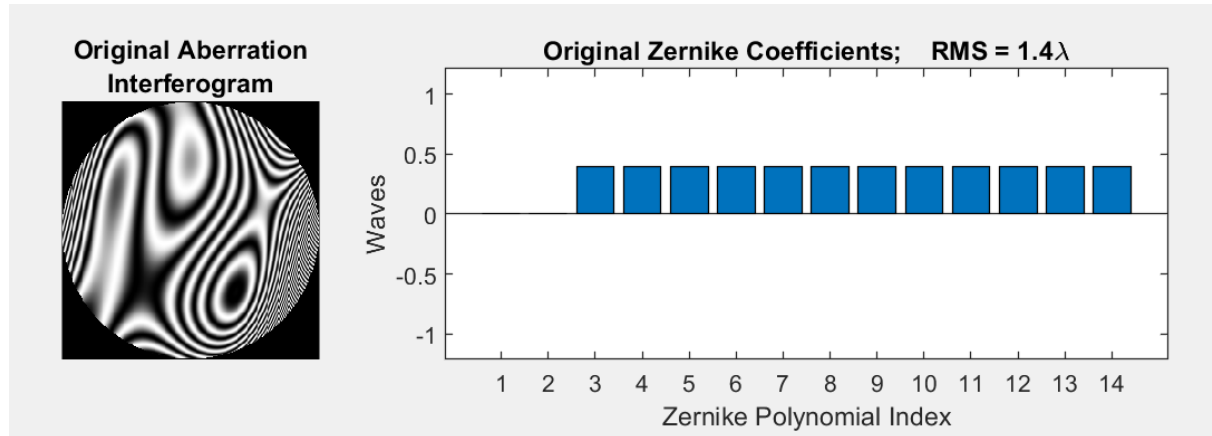


Fig. S2: Artificially generated wavefront with constant Zernike polynomials values

DIAM. [mm]	Initial RMS (waves @530nm)	Residual RMS (waves @530nm)
1	1.4	0.03
1.5	1.4	0.21
2	1.4	0.57
2.5	1.4	0.82
3	1.4	1.1
3.5	1.4	1.2

Table T1: Wavefront Reconstruction accuracy in function of the sub-pupil diameter.

Results comparison against the ground truth.

In this section, we compare the results of the isoplanatic (ISO) and anisoplanatic (ANI) deconvolutions with respect the ground truth image obtained without the aberrating phase plate. Both reconstructions were obtained by deconvolving the aberrated image. We restrict this analysis on the cropped region reported in the Fig.4 in panels 4d (ground truth), 4e (ISO), and 4f (ANI).

For each reconstruction, we compute the average percentage difference between the ground truth image I_G and the ISO and ANI, defined as:

$$d(I_G, I_{\{ISO, ANI\}}) = \frac{1}{N_{pixel}} \sum \frac{|I_G - I_{\{ISO, ANI\}}|}{I_G}.$$

In our reconstructions, we obtain $d(I_G, I_{ISO}) = 15.9\%$ and $d(I_G, I_{ANI}) = 10.6\%$. The anisoplanatic reconstruction turns to be better than the isoplanatic one because it gets closer to the ground truth. In Fig.S3 we report the map of the pixel-wise percentage difference for each ground truth-(ISO/ANI) pair corresponding to Fig.4cdef.

The ISO deconvolution introduces low-noise artifacts spread through the whole image and this gives the perception of more contrast in the final reconstruction. In both panels, the region where the error is higher is the dark region in which the sample is not present (bottom right).

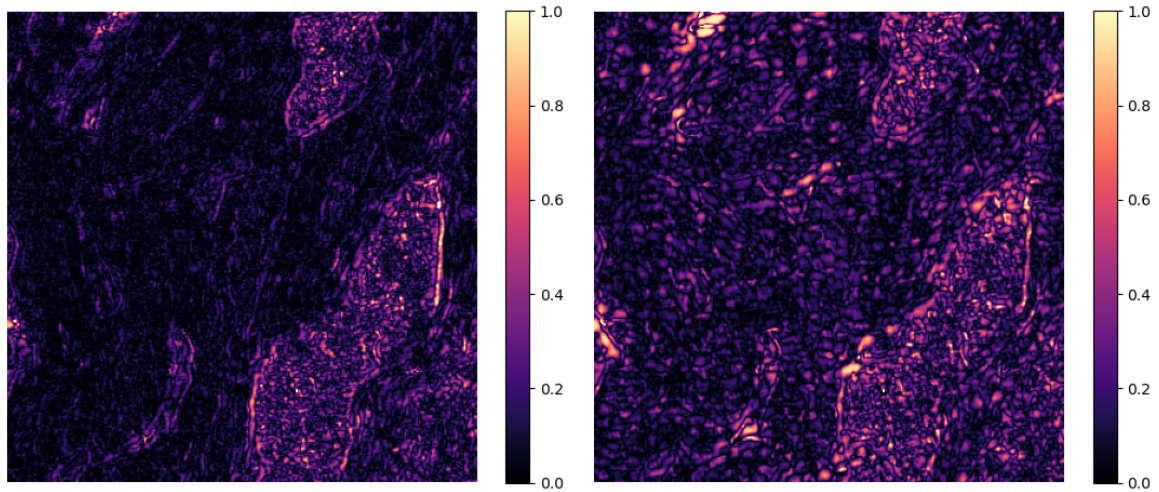


Fig. S3: Left panel, percentage difference between the ground truth and the ANI reconstruction. Right panel, percentage difference between ground truth and ISO reconstruction.

[1] J. Mocci, M. Quintavalla, C. Trestino, S. Bonora and R. Muradore, "A Multiplatform CPU-Based Architecture for Cost-Effective Adaptive Optics Systems," in IEEE Transactions on Industrial Informatics, vol. 14, no. 10, pp. 4431-4439, Oct. 2018, doi: 10.1109/TII.2018.2799874.